

In Situ Optical Monitoring of the Electrochemical Conversion of Dielectric Nanoparticles: From Multistep Charge Injection to Nanoparticle Motion

Jean-François Lemineur, Jean-Marc Noël, Alexa Courty, Dominique Ausserré, Catherine Combellas, Frédéric Kanoufi

▶ **To cite this version:**

Jean-François Lemineur, Jean-Marc Noël, Alexa Courty, Dominique Ausserré, Catherine Combellas, et al.. In Situ Optical Monitoring of the Electrochemical Conversion of Dielectric Nanoparticles: From Multistep Charge Injection to Nanoparticle Motion. Journal of the American Chemical Society, 2020, 142 (17), pp.7937-7946. 10.1021/jacs.0c02071 . hal-03026551

HAL Id: hal-03026551
https://hal.science/hal-03026551

Submitted on 26 Nov 2020

HAL is a multi-disciplinary open access archive for the deposit and dissemination of scientific research documents, whether they are published or not. The documents may come from teaching and research institutions in France or abroad, or from public or private research centers.

L'archive ouverte pluridisciplinaire **HAL**, est destinée au dépôt et à la diffusion de documents scientifiques de niveau recherche, publiés ou non, émanant des établissements d'enseignement et de recherche français ou étrangers, des laboratoires publics ou privés.



Distributed under a Creative Commons Attribution - NonCommercial - ShareAlike 4.0 International License

In Situ Optical Monitoring of the Electrochemical Conversion of Dielectric Nanoparticles: from Multi-Step Charge Injection to Nanoparticle Motion

Jean-François Lemineur,[1,2] Jean-Marc Noël,[1] Alexa Courty,[2] Dominique Ausserré,[3] Catherine Combellas,[1] Frédéric Kanoufi[1,*]

1 Université de Paris, ITODYS, CNRS-UMR 7086, 15 rue Jean-Antoine de Baïf, 75013 Paris, France.

2 Sorbonne Université, MONARIS, CNRS-UMR 8233, 4 Place Jussieu, 75005 Paris, France.

3 Université du Maine, Institut des Matériaux et Molécules du Mans, CNRS-UMR 6283, Avenue O. Messiaen, 72000 Le Mans, France.

ABSTRACT: By shortening solid-state diffusion times, the nanoscale size reduction of dielectric materials -such as ionic crystals- has fueled synthetic efforts towards their use as nanoparticles, NPs, in electrochemical storage and conversion cells. Meanwhile, there is a lack of strategies able to image the dynamics of such conversion, *operando* and at the single NP level. It is achieved here by optical microscopy for a model dielectric ionic nanocrystal, a silver halide NP. Rather than the classical core-shrinking mechanism often used to rationalize the complete electrochemical conversion and charge storage in NPs, an alternative mechanism is proposed here. Owing to its poor conductivity, the NP conversion proceeds to completion through the formation of multiple inclusions. The super-localization of NP during such heterogeneous multiple-step conversion suggests the local release of ions, which propels the NP towards reacting sites enabling its full conversion.

INTRODUCTION

Nanoparticles, NPs, are key components in many electrochemical devices and applications related to energy conversion or storage,[1] such as photovoltaics,[2] batteries,[3] fuel cells or (photo)electrolyzers for the electrocatalytic activation of small molecules (from water splitting to CO_2 reduction).[4]

Ionic crystals, metal oxides or polymers, which are dielectrics in the visible range, have long been discarded from electrochemical cells owing to their poor electronic and/or ionic conductivities. However, these materials have also benefited from nanoscale size reduction, which predominantly shortens solid-state ion diffusion times, allowing charge transfer.[5] In batteries, this strategy is used to reach ultimate charge storage capacity, as illustrated from the promises of $LiFePO_4$ nanocrystals as a cathode material.[6] Such opportunity fuels synthetic efforts towards new dielectric nanomaterials able to meet the needs of electrochemical storage or conversion cells with higher capacity conversion and faster rates.

The performances of nanomaterials in electrochemical cells are usually probed within an ensemble, electrically connected through additives to a current collector. However, a rational consideration of the intrinsic performances of NPs for energy storage and conversion applications requires probing and imaging intrinsic electrochemical activity or conversion, at the single NP level, particularly under operating conditions. Different single NP electroanalytical strategies have been proposed,[7,8] although rarely for the electrochemical study of dielectric materials.[5,9-13] A strategy consists in catching the electrochemical activity of a polarized ultramicroelectrode (UME, a microsized current collector) during the stochastic collision of dispersed colloidal NPs.[9,14,15] The current transient recorded for each stochastic event reflects either the adsorption dynamics of inactive NPs,[9] or the storage capacity associated to the electrochemical conversion of electroactive NPs.[10] However, for colloids in solution, the current transients are convoluted to their intrinsic Brownian motion, resulting in multiple discrete sub-events difficult to interpret -if not- by the partial transformation and discrete residence of the NP onto the UME.[16,17]

Although insightful, such situation drastically differs from the behavior of NPs immobilized on or confined at an electrode for which electrochemical imaging strategies are more appropriate. Scanning electrochemical nanoprobes (nanoelectrodes or nano-electrochemical cells) are able to produce high resolution mapping of individual nanomaterials[18] or to address the charge storage capacity of battery material by inspecting transient (de)intercalation processes at the single particle level.[11,12] These processes are often associated to longer characteristic times which are delicate to track from current transients, unless by confining the event in a microreactor (such as emulsion droplets)[19] or a sub-micrometric electrochemical cell.[11] Moreover, these intrinsic electrochemical activities are often associated to structural dynamic changes, such as deformation, volume expansion, dissolution, etc…, difficult to visualize without a complementary microscopic observation. Apart from AFM imaging,[20] or *in situ* TEM,[21] often restrictive owing to the slowness of the scanning imaging process or to e-beam dose perturbations, high resolution optical microscopies offer high throughput, quantitative and dynamic analysis of single NPs electrochemistry.[22] They afford complementary *in situ* mechanistic insights into various phenomena ranging from

chemical transformations (double layer charging,[23-25] NP conversion,[13,22,26-33] nanobubbles electrogeneration[34]) to motion,[26c,27] or local polarization due to structural changes[24,25,32,33] associated to the electrochemical actuation of NPs. Although powerful these strategies have been mostly applied to plasmonic nanomaterials and more rarely employed to depict the electrochemistry of dielectric NPs.[13]

Herein, the dynamics of the charge storage by electrochemical conversion of individual surface-confined ionic nanocrystals is monitored optically. Ionic nanocrystals are poor electronic conductors, and their electrochemical conversion, into a more conducting material, can be a source of irreversibility during the cycling process. Indeed, as illustrated in Figure 1, if conducting NPs (or NPs capped with a conducting binder) are expected to convert through a spherically symmetric core-shrinking mechanism, dielectric NPs will follow a strongly anisotropic conversion route: the conversion would start from the contact with a current collector through an inclusion formation. This is devised from a simulation study in the first part of this work, showing that, from an electrochemical point of view, if both situations may present different simulated characteristic transformation rates, they are difficult to differentiate experimentally. However, based on the differing symmetry of each transformation scenario, the intermediates involved, and therefore the conversion mechanism, should be discriminated from their optical response. To decipher such mechanistic scenarii, it is pertinent monitoring in real time and *in situ*, by high resolution optical microscopy, the electrochemical conversion of dielectric NPs. This relies on the choice of both a model dielectric NP and a highly sensitive label free optical microscopy able to image *in situ* these dielectric NPs. The latter is afforded by interferometric-based techniques.[29b,c,35] The Backside Absorbing Layer Microscopy (BALM)[29b,c] is chosen as it uses ultrathin Au coated glass sample surfaces, which are, as presented in Figure 1, both an optical and electrochemical sensor of NPs (experimental details given in Supporting Information, SI, Section SI1). As for the former model dielectric material, a colloidal silver halide, AgX nanocrystal (here either X = Cl or Br, see SI, Section SI1), was chosen because both AgX and its reduction product, Ag, have well documented optical properties,[36,37] which are more appropriate to devise, from optical response prediction, the different scenarii occurring during the solid-state conversion:

$$AgX + e^- \rightarrow Ag + X^- \quad (1)$$

The understanding of the solid-state conversion of silver-ion based dielectric nanocrystals is of interest for energy conversion or storage.[38] The partially converted AgX/Ag hybrid NPs are attracting photocatalysts of CO_2 reduction. Moreover Ag_2O NPs analogues are commonly used in Zn/Ag high density and high power batteries. The strategy developed herein will directly apply to apprehend such systems, and should be extended, in future works, to less optically explored dielectric NPs.

This work proposes to unravel optically the storage of charge associated to the conversion of AgX into metallic Ag by investigating if it proceeds by a spherical symmetric, radial core-shrinking, or through the formation of inclusions. By tracking the NP optical response and super-localizing its position during its electrochemical conversion at the BALM electrode, we are able to decipher, *operando*, the dynamics of the solid-state transformation of individual dielectric NPs. The NP conversion is also associated with the production of local ion fluxes, which are probed from the motion of the NP during its conversion.

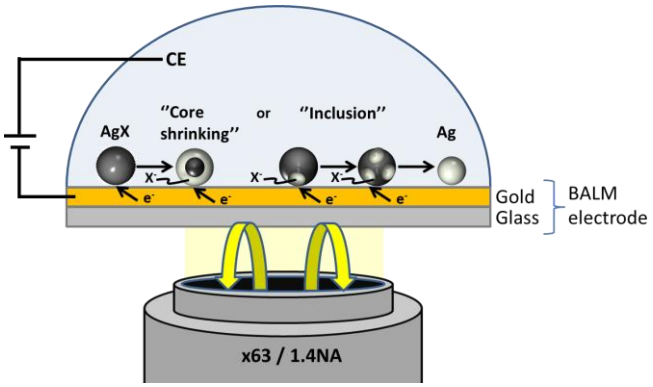


Figure 1. Monitoring the dynamics of the electrochemical conversion of individual dielectric NPs. The different ways of conversion of a model dielectric material, here AgX which converts into metallic Ag, by radial core-shrinking or formation of heterogeneous inclusions.

RESULTS AND DISCUSSION

Modelling Single NP Electrochemical Conversion Mechanims. The dynamics of the electrochemical conversion of a single NP contacting a planar electrode was simulated as a diffusion reaction process described in SI, section SI2, by finite element method (COMSOL®) in Figure 2. Two cases, usually encountered during the conversion of battery-active NPs,[39] are considered (Figures 1 and 2).

In the first one (the "radial core-shrinking model"), the outer region of the AgX NP is reduced into metallic Ag through a shell formation while the AgX core shrinks with time (Figure 2a). This corresponds to the case of a perfectly conducting NP whose external surface is equipotential, usually depicted in batteries owing to the presence of conductive binder coating the nanostructured electroactive materials.

The second one relies on the anisotropic growth of an Ag "inclusion" at the NP-electrode contact (Figure 2b) producing a Janus type NP.

Figure 2a and b presents the simulated AgX concentration (black region), and equivalently Ag concentration (white region), profiles in the NP at different conversion times according to either the core-shrinking or the single-inclusion Janus model. As expected, each mechanism yields intermediates that present either a spherical or an axial symmetry. The different mechanistic situations were then compared based on their respective characteristic conversion time, namely the time needed to convert half the NP material. As sketched in Figure 2, from geometric consideration, the half-conversion, $\delta \approx 50\%$, of a NP of diameter d_0 corresponds to transport through either a shell of thickness $l_{1/2,CS} \approx 0.15 \times d_0$ in the core-shrinking model or $l_{1/2,} \approx 0.8 \times d_0$ for the inclusion formation.

In silver-based crystals thin films, despite great variability in values, the diffusion of Ag^+ is mostly limiting, with D values at maximum in the $10^{-11} cm^2/s$,[40] comparatively to halide ions, which diffuses about 10 times more slowly than in solution.[41] For a purely diffusion limited process, with concentration profiles given in SI, Figure SI2.1, the core-shrinking conversion half-time, $\tau_{1/2} = l_{1/2}^2/D$ would take about $\tau_{1/2,CS} \approx 0.2$s

and would be faster by more than 20-fold than that implying the formation of a single inclusion ($\tau_{1/2,J}$≈6s).

As seen in Figure 2, the model, described in SI, Section SI2, also takes into account a propagating interface within the NP between the unconverted and converted materials and the extent of ion expulsion in solution. For this purpose, the model considers not only the diffusion of ions in the NP but also the occurrence of electron hopping. Electron hopping, often suggested for explaining conduction in polymer electrolytes and other percolated systems,[42] allows accounting for the production of a conducting material, which modifies the contact-line between unconverted and converted materials within the NP volume. It is described by a homogeneous chemical reaction between the converted and unconverted materials within the NP, characterized by a rate k_{ex}.

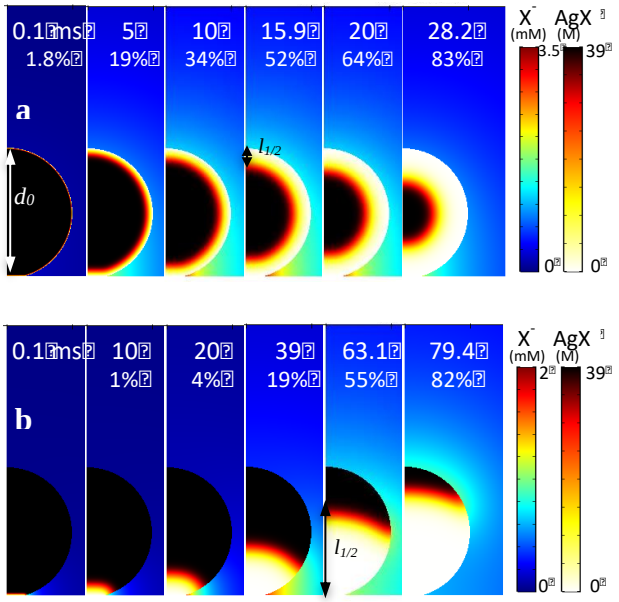


Figure 2. Comsol® simulation of the conversion dynamics of a 100nm AgCl NP (half of it is represented) contacting an electrode (lower plane) according to (a) the core-shrinking mechanism or (b) the formation of a single-inclusion Janus NP. Examples of successive concentration profiles (time in ms and conversion, δ, given) of AgCl in the NP and Cl^- ions expelled in the surrounding solution during the conversion. Simulations were obtained for solid phase diffusion D= 10^{-11} cm^2/s and a characteristic rate for electron hopping k_{ex}=$300s^{-1}$.

The electron hopping produces much faster conversion than if only the solid-state diffusion limitation was considered,[43] and it therefore particularly accelerates the single inclusion conversion. Indeed, as shown in Figure 2, implementing the interface propagation reduces the conversion half-times for both mechanisms to the sub-100ms range ($\tau_{1/2,CS}$=14ms and $\tau_{1/2,J}$=60ms for the core-shell and single-inclusion mechanisms respectively with k_{ex}=$300s^{-1}$). A perfect charge percolation would engage a hopping rate limited by physical diffusion within adjacent centers, separated by a=3.5Å, the interatomic distance, for example, in AgCl. This upper rate is given by Smoluchovsky theory as $k_{ex,lim}=8\pi D a N_A/V_{m,AgCl}$=$1.4x10^5$ s^{-1} with N_A the Avogadro number and $V_{m,AgCl}$ the molar volume of AgCl crystal. Extrapolating the simulations of Figure 2 to such limit yields $\tau_{1/2,CS}$=0.5 and $\tau_{1/2,J}$=3ms for the fastest conversion half-times for each mechanism (see SI, section SI2).

Overall, except likely for the >1s long diffusion limited conversion in the absence of electron hopping, the half-time conversion values are within reach of state-of-the-art electrochemical single entity studies. It should be interesting designing single entity electrochemical studies to allow differentiating all those mechanisms based on conversion current transients or $\tau_{1/2}$ values (see SI, section SI2). However, owing to the strong variability in the solid state ionic diffusion coefficients, and to the similarities in simulated features (see SI, Section SI2), we believe it is currently difficult to differentiate both mechanistic routes from single NP electrochemical measurements. We then propose to recourse to a complementary optical monitoring.

Optical Differentiation of AgX and Ag NPs. Colloidal solutions containing a 3:2 mixture of d_0 ~ 100 nm diameter CTAB capped AgCl and AgBr NPs were prepared[38,44] as described in SI (Figure S1.1 in Section SI1 in SI). The unimodal size distribution suggests AgCl and AgBr NPs cannot be differentiated by SEM images. The comparable values of AgCl and AgBr refractive indexes also suggest (see discussion in SI, Section SI1) they cannot be differentiated optically. All NPs detected optically were shown to present the same behaviors, suggesting that the processes described apply statistically equivalently to either AgCl or AgBr. Indeed, the conversion was studied here at sufficiently negative potential to ensure mass transfer limited conversion of either material, preventing also an electrochemical differentiation. Therefore, the NPs are denoted AgX throughout the manuscript.

To resolve the dynamics of the electrochemical conversion of individual AgX NPs, the latter should first be adsorbed on the Au BALM electrode. To favor the NP adsorption, the AgX NP solution was diluted 100 times in a NaCl solution (0.05M). It resulted in the destabilization of the colloidal solution, leading to the irreversible adsorption of the NPs on the electrode surface.[45]

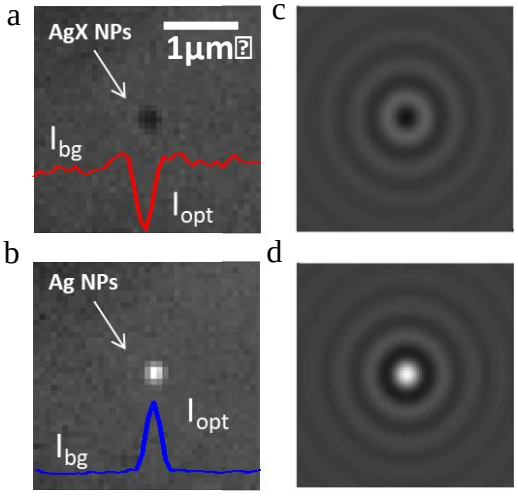


Figure 3. (a,b) BALM images of an adsorbed AgX NP and once reduced into an Ag NP. (c,d) Simulated 4x4µm² interferometric optical images at λ=510nm of a 100nm AgX NP and a fully converted 73nm Ag NP.

An example of monitoring of NP adsorption/conversion is given in the Supplementary Video (SI) summarized in Figure 3a and b. The AgX NP adsorptive impact on the electrode is

detected optically (Figure 3a) thanks to the appearance of a diffraction-limited dark contrast feature, I_{opt}–I_{bg}<0, where I_{opt} is the optical intensity of the contrast feature and I_{bg} the background level. Even though the BALM electrode is biased at a sufficiently negative potential to allow, when the AgX NP hits the surface, its reduction into Ag, the NP spot, remains dark for ~4s before a change to a bright contrast feature is detected (I_{opt}–I_{bg}>0, Figure 3b).

Such optical contrasts are predicted from an optical model adapted from that developed by the Ünlü's group,[35c,46] using the MNPBEM toolbox[46] (details in SI, Section SI3), for quantitatively interpreting single NP images obtained by interferometric-based microscopies. Figure 2c and d presents the simulated optical interferometric images for two NPs adsorbed on an Au BALM electrode: a 100nm AgX NP and a 73nm Ag NP (considering the NP volume change upon full AgX to Ag conversion). The model predicts with a good quantitative agreement in I_{opt}–I_{bg} values that dielectric AgX NPs adsorbed on the optical sensor appear as dark contrast features while metallic Ag NPs appear as bright contrast features.

NP Conversion from Simulated Optical Responses. Differentiating optically the fully unconverted and fully converted NPs is fruitful, the dynamics of the conversion may also be reached through such complementary monitoring. Owing to the difference in composition and symmetry, the AgX@Ag core-shell and the Janus-like Ag-inclusion in AgX intermediate NPs are expected to present different electronic and therefore optical properties. Differences in the localized surface plasmon resonance modes or their localization are expected. These differences should be unravelled from changes in scattering spectra,[37] estimate of the absolute NP polarizability, for example from complementary measurement of optical intensity and phase,[47] or super-localizing displacement of the scattering centroid.[24,25,32] The potentiality of an interferometric probing is evaluated from the simulated optical responses, I_{opt}, of the scattering properties of single NPs at a BALM electrode, which are compared to experimental data. The mechanistic strategy proposed here would apply identically to other complementary or richer optical information (such as spectroscopic or phase and amplitude).

The I_{opt} response of AgX@Ag core-shell and of a Ag-inclusion in AgX NPs were simulated for different NP conversions δ (see Section SI3 in SI). The NP with Ag inclusion is modeled overall as a sphere, as depicted in Figure 4a, in which the Ag inclusion is the assembly of two identical sphere-caps facing the gold electrode. The volume of Ag material, either as an inclusion or as a shell, was estimated from δ.

The simulated variations of I_{opt} with δ for the core-shell or single inclusion Janus models are presented as the black and orange curves, respectively plain and dashed, in Figure 4a. Both models show that upon conversion the optical contrast, I_{opt}-I_{bg}, of the NP is changed from dark (negative contrast) to bright (positive contrast) feature and with an overall increase in absolute value of the contrast. The core-shell model suggests a strong (>20x) contrast enhancement from the early beginning (δ>10%) of the NP conversion. If a strong contrast enhancement is also observed for the Janus model, it is reached more progressively and for larger δ values (δ>25%). As it will be discussed later on, the super-localization of the NP scattering centroid allows probing the NP displacement during its electrochemical transformation. The rotational motion of the axisymmetric Janus NP is expected to affect its optical response, I_{opt}, while not affecting that of the spherical symmetric core-shell NP (see discussion and simulated results for 90° or 180° rotated Janus NP in SI, Section SI3). Indeed, upon rotation, the Ag inclusion is pulled away from the Au electrode, lowering their coupling. Then a rotation of the Janus NP would tend to decrease I_{opt}. However such rotation also makes the overall situation more complex: once the inclusion is rotated, a new unconverted (AgX) part of the NP is now facing the electrode allowing the electrochemical formation of a new inclusion.

The formation of multiple inclusions is often suggested[48] for charge propagation in poorly conducting AgX materials. It invokes heterogeneous localized transformations similar to those observed during the reverse solid-state oxidation of Ag but into Ag oxides.[32] It is supported from SEM inspection, in Figure 4b, of AgX NPs adsorbed on the gold surface and submitted to a 4s short reduction pulse. As seen clearly on the magnification of Figure 4b and confirmed for >90% NPs (n=30 NPs), different brighter regions (metallic inclusions) are present on the NPs. Interestingly, their location opposite to the electrode surface as in the magnification of Figure 4b, suggests that the NP has rotated during the electrochemical process.

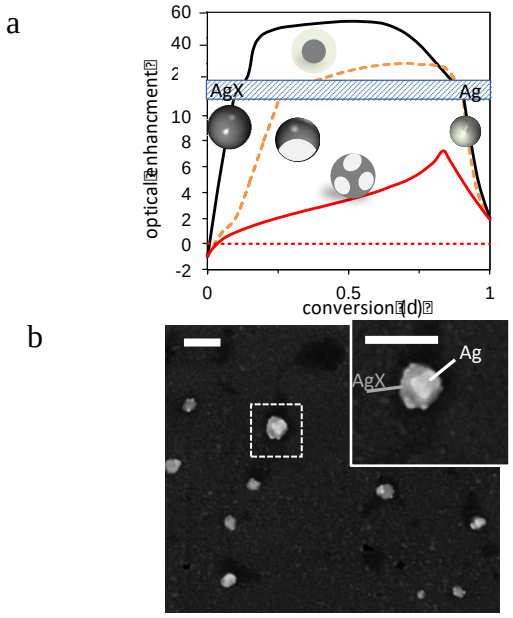


Figure 4. Towards optical quantitative imaging. (a) The simulated I_{opt} variations with δ, the AgX NP conversion into Ag, assuming the formation of a core-shell structure (black), or of a single inclusion Janus-type NP (dashed orange), or multiple mean-field inclusions (red); background level: dotted red line. (b) SEM images of AgX NPs adsorbed on the gold electrode surface after a 4s partial reduction: multiple Ag inclusions appear over the AgX NPs suggesting rotational motion of the NPs during the reduction (a 180° rotation for the large one shown in the magnified dashed region); scale bars = 200nm.

Simulating the optical response of such multiple inclusions situation is quite speculative without prior knowledge of the number and distribution of the mosaic of inclusions during the NP conversion. An alternative is to consider it in a mean field approach, which can be simulated by considering a plain composite Ag/AgCl NP characterized by an apparent refractive index estimated, as a first guess, from the effective medium

theory (see discussion in SI, Section SI3).[49] The red line in Figure 4a shows the resulting simulated I_{opt} variations with δ: the contrast enhancement increases more progressively and to a much lower maximum value (7x times at 85% conversion).

It is further confirmed experimentally from the dynamic optical monitoring of the electrochemical conversion of individual AgX NPs: the experimental I_{opt} and I_{bg} intensities were measured over the reduction time, and compared to the optical simulations. A typical example of I_{opt} transient is given in Figure 5, while other examples are given in SI, Section SI4.

First, the experimental intensities at the beginning, δ = 0, or end, δ = 1, of the process are in good agreement, compared to the background level (experimental: blue line, simulated: red dashed line) with the simulated one (red solid line). Then, the maximum optical contrast enhancement (approx. 6x at the plateau in Figure 5) never exceeded an 8x factor for n>20 NPs, which disqualifies the core-shell mechanism or single-inclusion models and supports the mechanism based on multiple silver inclusions.

Using the simulated I_{opt}–δ variations from the mosaic inclusion model, a quantitative assignment of the dynamics of the AgX NP conversion, δ(t), is at hand for interpreting the experimental I_{opt} transients. An illustration is given in Figure 5a (symbols) showing an overall almost complete conversion of the NP, with a first fast stage (up to 80% conversion) with approx. first order transformation rate of 0.8 s^{-1}. Later on, the full NP conversion is reached with a ten times slower kinetics.

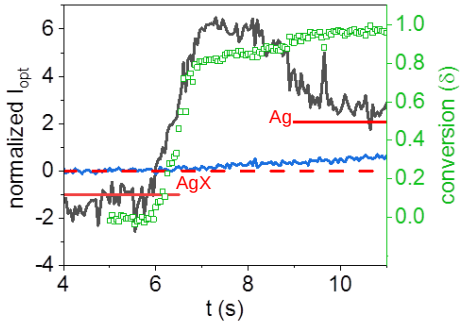


Figure 5. Optical transient, I_{opt}–t, recorded during the reduction of a single AgX NP adsorbed on a BALM electrode; experimental background in blue. Simulated optical contrast changes of the NPs (red lines) for δ = 0, AgX, and δ = 1, Ag, compared to the simulated background (dashed red line) and the conversion kinetics extracted from the Ag inclusion simulation (□).

Resolving a Conversion in Multiple Steps. The transformation of the NPs adsorbed on the surface is close to completion but is surprisingly slow (>3s). This value disqualifies the core-shrinking mechanism. It seems consistent with the simulated value of $\tau_{1/2,J}$ ≈6s for the diffusion limited growth of a single inclusion (see SI, Figures SI2.1 and SI2.2) with limited influence of electron hopping. However the distinct separation between the regions corresponding to either the Ag inclusion or the AgX material in the SEM image of Figure 4b rather supports the propagation of a front of converted material, in line with the electron hopping scenario. The observation in Figure 4b of multiple inclusions and their location far from the electrode contact, suggests the importance of the NPs/surface interaction and of the relative motion of the NP on the electrode that result in the formation of multiple electrochemical steps during conversion.

Such multiple steps transformation is becoming a key feature in single NP electrochemistry, revealing the complexity of NP motion during their electrochemistry. It was evidenced in electrochemical nanoimpact studies of the oxidation of Brownian Ag NPs.[16,17] By increasing the experiment time resolution, closely separated successive sub-ms current spikes were resolved corresponding to successive partial electrodissolution steps of a single NP.

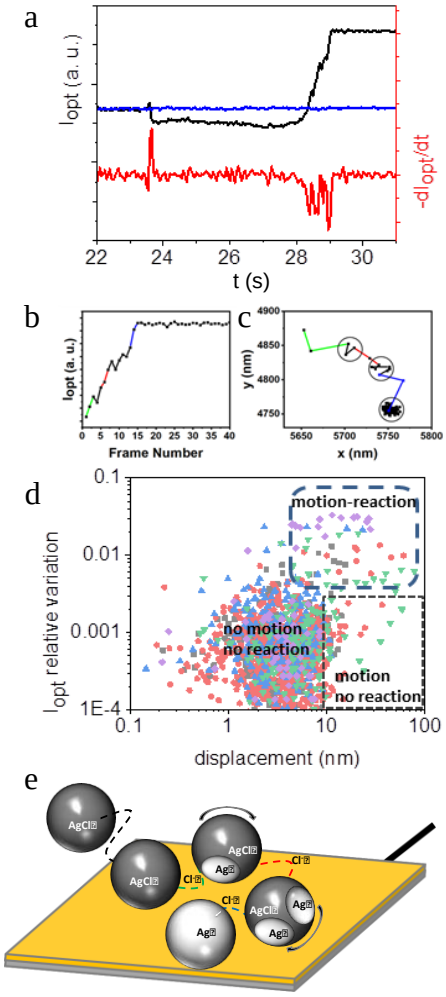


Figure 6. (a) Resolving multistep reductive conversion of surface confined AgX NPs and derivative of the I_{opt} transient, showing the discrete NP conversion (background in blue). (b) Zoom in the I_{opt} transient presented in (a) during the time when the NP appears as bright contrast feature. (c) Motion of the NP tracked by super-localization and correlated to the intensity transient in (b). (d) Scatter plot representing the relative variation of I_{opt} and displacement recorded during the conversion of 5 AgX NPs. The limit for reaction occurrence is 0.5% variation in I_{opt}; motion is assigned to NP displacement >7nm. (e) Scheme of the multi-step path of a NP fueled by halide ion release.

Multiple step electrochemical process was also suggested for NPs adsorbed on electrodes and for slower processes such as those involved in corrosion or amorphous solid phase transformation. The dynamics of the slow transformation of individual adsorbed NPs is difficult to cope by direct electrochemical techniques. The slow electrochemical conversion of redox active components inside >400nm attolitter emulsion droplets

could be tracked by electrochemical current transients.[19,43] However for the smallest converted material, comparable to that corresponding to the full conversion of a 100nm AgX NP (ca. 2pC), the electrochemical current sensitivity and baseline drift have not allowed depicting multi-step conversion. The use of confined electrochemical cell may allow increasing the electrochemical signal to noise ratio. An alternative consists in using a complementary signature of the conversion. The dynamics of slow conversion processes is within reach of optical microscopy.[26c,27] It was demonstrated during the dissolution of silver pseudo-halides (thiocyanates) NPs[28b] or during the oxidation of Ag into Ag_2O.[32]

Increasing the optical signal-to-noise ratio, I_{opt} transients reveal such dynamics, as in Figure 6a: a NP hits the polarized electrode at t=23.8s, then begins to react after ~4s delay time. I_{opt} transients present a continuous increase >1s and further levelling showing a fast conversion of the NP but halting at ca. 80%, based on the optical simulation. The first time-derivative of I_{opt} (Figure 6a, red curve) mimics qualitatively the evolution of the electrochemical current that should be detected. It reveals several close-packed optical spikes (between 28 and 29s), suggesting multiple partial reduction events. It is also clear that the stepwise reactions are not due to "one-by-one" reduction of individual NPs trapped in agglomerate. Indeed, agglomerates can be optically dismissed as they are characterized by an abnormal intensity in comparison with those of single AgX NPs, which always possess similar intensities when hitting the electrode surface.

Identifying NP Motion during its Conversion. This hypothesis was tested by scrutinizing the displacement of the scattering centroid of the surface-confined NP during its transformation. The position of the centroid of the NP (regardless of its contrast) was super-localized and tracked in two dimensions with sub-pixel accuracy by using the Crocker and Grier's centroid finding algorithm (see Figure S5.1 in SI, Section SI5).[50] The resulting mean square displacement before and after the NP transformation is included in Figure S5.2.

Before the contrast modification (from 23.8 to 28s, Figure 6a), the NP moves over the surface with a restricted diffusion coefficient, D_{NP} = 5x10^{2}nm²/s, 4 orders of magnitude lower than in solution. It cannot be ascribed to solution diffusion; indeed even when considering the transport dampening within the viscous layers near the electrode surface, the diffusion of a 100nm NPs is expected to be dampened by no more than 25 times.[51] The hindered motion detected here rather shows the surface diffusion of the NP, by rotation or translation. During this motion the NP should find a position allowing its conversion by charge transfer, resulting in variations in I_{opt}. At the end of the reaction (>29s), the NP is not diffusing anymore, within the tracking precision, ±7nm. It corroborates that NP transformation is associated to its motion near the electrode surface.[26c]

Closer examination of the motion of the surface-confined NP during the I_{opt} variation, which corresponds to its electrochemical transformation, is also instructive. Figure 6b and c presents, respectively, the variation of the I_{opt} and NP position when the NP is detected as a bright contrast feature (higher signal to noise ratio).

During this period of time the centroid of the NP has moved by 160nm (it is by >200nm during its whole conversion, see SI, Figure S5.4 in Section SI5). The overall travelling distance larger than the NP dimension cannot be explained by the probing of a local polarization change of the NP, such as those expected during the formation of an asymmetric NP structure.[24,25,32] Indeed the optical modeling of such situation confirms that it would induce a relocalization of the scattering centroid by no more than the NP dimension (see SI, section SI3). It rather suggests the motion of the NP over the electrode. The rotation of the NP is the most likely, and the l > 200nm overall motion length of the centroid suggests a rotation of the NP by an angle of lx360°/πxd_0 > 230°.

The dynamics of this motion is also accessible. The colored segments in Figure 6c are related to time durations when the highest variations in I_{opt} are detected (dI_{opt}/dt spikes in Figure 6a red curve), corresponding to the highest probable transformation current, while the black segments are assigned to approx. unchanged I_{opt} values.

Noteworthy, in Figure 6b, when the NP shows the lowest I_{opt} variations, the NP position is almost unchanged within the precision of the super-localization (±7nm, represented as the dark circles in Figure 6c). Such correlation between I_{opt} variations and NP motion is found for all adsorbed NPs experiencing a conversion (n>10 NPs, see other examples in Figure S5.3, SI, Section SI5).

This is summarized for n=5 NPs in the scatter plot showing, in the zone diagram of Figure 6d, the instant I_{opt} relative variation and displacement of individual NPs. Different zones are clearly identified depending on whether reaction and/or motion are detected. These results allow us proposing a mechanism for the dynamics of the NP transformation (Figure 6e). The NP is pinned within an electrochemically inactive position or configuration from which it is either trapped (the most probable situation in the no-motion/no-reaction zone) or may diffuse in search for active regions (motion/no-reaction zone). Once charge transfer occurs, which is probed by I_{opt} variations, the NP is submitted to >7nm motion over the electrode (motion/reaction zone), suggesting that the NP electrochemical transformation is associated to a propulsion force.

The motion of single NPs during electrochemical actuation was also suspected in earlier stochastic electrochemical studies;[9d,28b,52] the extent of such motion was also demonstrated from the sub-100nm displacement of catalytic NPs probed *ex situ* by same location SEM images.[53] The authors also imply and simulate different phoretic mechanisms to explain the dynamic changes of electrodes made of assemblies of NPs. Here, the motion is extended to transient processes: a catalytic reaction at a NP can be sustained for much longer times than the (irreversible) conversion of a NP material. Noteworthy optical microscopy provides a unique means to probe such transient motion in real time and *in situ* with 10nm spatial resolution through optically correlated transformation/motion events. As for the explanation of the motion, the simulation of the conversion processes given in Figure 3 also suggests a local gradient of X^- ions. Whatever the transformation mechanism explored in Figure 3 >2mM ions are expelled within the NP-electrode contact region at the onset of the conversion. As the transformation is highly dynamic and likely does not imply a single inclusion, simulating such effect seems speculative. However, the local release of ions during the chemical transformation of a particle is commonly observed in nanomachines and used for their propulsion.[54] It has been recently detected in a closely related AgCl-coated Janus polymer microbeads: upon photoreduction of the AgCl layer, Cl^- anions are expelled driving a diffusiophoretic motion of the particles

with velocities in the µm/s range.[55] The lower velocities detected here (>0.2 µm/s) are consistent with a drag force exerted by the interaction of the NP with the substrate. By analogy, we suggest that the local electrochemical reduction of the AgX NP actuated at the electrode-NP interface locally releases X^- anions enabling the diffusiophoretic NP motion. The motion temporization is again detected as the NP is pinned to a new electrochemically inactive region, searching again for a better electrochemically active configuration. Successive phases of electrochemical activations and pinning halts are experienced until the NP transformation is completed. Noteworthy the NP-electrode interaction is stronger than the phoretic NP desorption and irreversible loss in solution.

The multi-step partial oxidation of Ag colloids[16,17] was assigned to their increased mobility owing to a decrease in size upon oxidative dissolution. The decrease in size is comparatively marginal during the AgX to Ag reduction. Partial reduction events have an alternative origin related to the poor conductivity of the AgX material. It is consistent with the poor cycling and storage capacity decay usually reported for battery cathodes made of poorly conducting metal oxide nanostructures. In line with the optical model in favor of a heterogeneous conversion through inclusions, it suggests the loss of conductive contacts within the NP. The duration of the multiple reduction steps may then be related to the occurrence of electrical connections between the NP and the electrode:[26c] for Brownian and highly mobile NPs, the probability of NP multiple contacts is much higher than for surface-confined NPs.

CONCLUSION

The electrochemical conversion of NPs made of dielectric or poorly conducting materials is of increasing relevance in energy storage devices. The dynamics of such electrochemical transformation is studied here *operando* at the single NP level, for a model system: colloidal AgX NPs adsorbed on a highly sensitive BALM opto-electrochemical sensor. The simulated transport reaction processes within the NP suggests that the NP conversion would be difficult to differentiate from state-of-the-art single NP electrochemical study. It is suggested here that an optical monitoring supported by optical models allows differentiating the conversion mechanisms and quantifying instantaneously the transformation rate of AgX NPs.

The reduction of AgX NPs proceeds through the formation of multiple Ag inclusions rather than of the homogeneous growth of a conductive Ag shell and shrinking of the AgX core. Although this demonstrates the difficult formation of conductive paths within dielectric NPs in the absence of the conductive binder used in battery electrode preparations, the reduction still proceeds up to the full NP conversion, but through multiple contacts with the electrode, *i.e.* multiple reduction steps. This suggests a relocalization of the NP during its conversion and explains the relatively long conversion time, which scales as several seconds. It contrasts with the usually much faster (by 3 orders of magnitude) electrochemical transients coped in studies relying on the electrochemical collisions of single colloidal NPs on an electrode. It suggests that the latter may not suitably picture the electrochemistry of poorly conducting NPs under real conditions, particularly those where NPs are connected to a current collector.

Finally, super-localizing the NP during its conversion allows evidencing the origin of the multiple reduction steps. Its motion on the electrode is associated to its electrochemical conversion. Such NP motion results from a local formation of an Ag inclusion, due to the poor AgX material conduction, fueled by local release of halide ions.

On one hand, the uncontrolled NP motion associated to the anisotropic electrochemical conversion of poorly conducting NPs may be a source of deformation of NP-based electrode materials. On the other hand, such motion enables multiple NP-electrode connections allowing to exploit the whole conversion and charge storage capacity (higher energy) of dielectric nanomaterials even in the absence of binder.

ASSOCIATED CONTENT

Supporting Information. The Supporting Information is available free of charge on the ACS Publications website.
Video showing a single AgX NP landing at a BALM electrode and its partial conversion into Ag NP. (AVI)
Additional information related to experimental details (NP synthesis, experimental setups), Comsol® EC simulation, optical model, complementary optical transients, EC nanoimpact experiments, NP motion analysis. (PDF)

AUTHOR INFORMATION

Corresponding Author

*e-mail: frederic.kanoufi@univ-paris-diderot.fr

Funding Sources

This work was financially supported by ANR NEOCASTIP ANR-15-CE09-0015-02 project, by Labex MiChem, part of the French state funds managed by the Agence Nationale pour la Recherche, ANR, within the Investissement d'Avenir program under reference ANR-11-IDEX-004-02, and through the CNRS and Paris Diderot University.

ACKNOWLEDGMENT

Nicolas Pageaud is warmly thanked for the artistic version of the graphical abstract.

REFERENCES

[1] Zhang, Q.; Uchaker, E.; Candelaria, S. L.; Cao G. Nanomaterials for energy conversion and storage. *Chem. Soc. Rev.* **2013**, *42*, 3127-3171.

[2] Huynh, W. U.; Dittmer, J. J.; Alivisatos, A. P. Hybrid Nanorod-Polymer Solar Cells. *Science* **2002**, 295, 2425-2427.

[3] Sun, Y;. Liu, N.; Cui Y. Promises and challenges of nanomaterials for lithium-based rechargeable batteries *Nat. Energy* **2016**, *1*, 16071.

[4] Seh, Z. W.; Kibsgaard, J.; Dickens, C. F.; Chorkendorff, I.; Nørskov, J. K.; Jaramillo, T. F. Combining theory and experiment in electrocatalysis: Insights into materials design. *Science* **2017**, 355, 1-12.

[5] Velmurugan, J. ; Zhan, D. ; Mirkin, M.V. Electrochemistry through glass. *Nat. Chem.* **2010**, *2*, 498-502.

[6] Gibot, P.; Casas-Cabanas, M.; Laffont, L.; Levasseur, S.; Carlach, P.; Hamelet, S.; Tarascon, J-M.; Masquelier, C. Room-temperature single-phase Li insertion/extraction in nanoscale Li_xFePO_4. *Nat. Mater*. 2008, *7*, 741-747.

[7] Hui, J.; Gossage, Z. T.; Sarbapalli, D.; Hernández-Burgos, K.; Rodriguez-López, J. Advanced electrochemical analysis for energy storage interfaces, *Anal. Chem.* **2019**, *91*, 60-83.

[8] Patrice, F. T.; Qiu, K.; Ying, Y.-L.; Long Y.T. Single nanoparticle electrochemistry. *Annu. Rev. Anal. Chem.* **2019**, *12*, 347-370.

[9] (a) Quinn, B. M.; Van't Hof, P. G.; Lemay S. G. Time-resolved electrochemical detection of discrete adsorption events. *J. Am. Chem. Soc.* **2004**, *126*, 8360-8361; (b) Fodsick, S.E.; Anderson, M. J.; Nettleton, E. G.; Crooks, R. M. Correlated electrochemical and optical tracking of discrete collision events. *J. Am. Chem. Soc.* **2013**, *135*, 5994-5997; (c) Dick, J. E.; Renault, C.; Bard, A. J. Observation of single-protein and DNA macromolecule collisions on ultramicroelectrodes. *J. Am. Chem. Soc.* **2015**, *137*, 8376-8379; (d) Boika, A.; Thorgaard, S. N.; Bard, A. J. Monitoring the electrophoretic migration and adsorption of single insulating nanoparticles at ultramicroelectrodes. *J. Phys. Chem. B* **2013**, *117*, 4371-4380.

[10] (a) Cheng, W.; Zhou, X.-F.; Compton, R. G. Electrochemical sizing of organic nanoparticles. *Angew. Chem. Int. Ed.* **2013**, *52*, 12980-12982; (b) Stuart, E.J.E.; Tschulik, K.; Batchelor-McAuley, C.; Compton, R.G. Electrochemical observation of single collision events: fullerene nanoparticles. *ACS Nano* **2014**, *8*, 7648-7654; (c) Zampardi, G.; Batchelor-McAuley, C.; Käthelhön, E.; Compton, R.G. Lithium-ion-transfer kinetics of single $LiMn_2O_4$ particles. *Angew. Chem. Int. Ed.* **2017**, *56*, 641-644.

[11] (a) Takahashi, Y.; Kumatani, A.; Munakata, H.; Inomata, H.; Ito, K.; Shiku, H.; Unwin, P. R.; Korchev, Y. E.; Kanamura, K.; Matsue, T. Nanoscale visualization of redox activity at lithium-ion battery cathodes. *Nat. Commun.* **2014**, *5*, 5450; (b) Tao, B.; Yule, L. C.; Daviddi, E.; Bentley, C. L.; Unwin, P. R. Correlative electrochemical microscopy of Li-ion (de)intercalation at a series of individual $LiMn_2O_4$ particles. *Angew. Chem. Int. Ed.* **2019**, *58*, 4606-4611.

[12] (a) Snowden, M.E.; Dayeh, M.; Payne, N. A.; Gervais, S.; Mauzeroll, J.; Schougaard, S. B. Measurement on isolated lithium iron phosphate particles reveals heterogeneity in material properties distribution. *J. Power Sources* **2016**, *325*, 682-689; (b) Dayeh, M.; Ghadivel, M. Z.; Mauzeroll, J.; Schougaard, S. B. Micropipette contact method to investigate high-energy cathode materials by using an ionic liquid. *ChemElectroChem* **2019**, *6*, 195-201.

[13] (a) Jiang, D.; Jiang, Y.; Li, Z.; Liu, T.; Wo, X.; Fang, Y.; Tao, N.; Wang, W.; Chen, H.-Y. Optical imaging of phase transition and Li-ion diffusion kinetics of single $LiCoO_2$ nanoparticles during electrochemical cycling. *J. Am. Chem. Soc.* **2017**, *139*, 186-192; (b) Linlin, S.; Jiang, D.; Li, M.; Liu, T.; Yuan, L.; Wang, W.; Chen, H.-Y. Collision and oxidation of single $LiCoO_2$ nanoparticles studied by correlated optical imaging and electrochemical recording. *Anal. Chem.* **2017**, *89*, 6050-6055;

[14] Xiao, X.; Bard. A. J. Observing single nanoparticle collisions at an ultramicroelectrode by electrocatalytic amplification. *J. Am. Chem. Soc.* **2007**, *129*, 9610-9612.

[15] Zhou, Y.-G.; Rees, N. V.; Compton. R. G. The electrochemical detection and characterization of silver nanoparticles in aqueous solution. *Angew. Chem. Int. Ed.* **2011**, *50*, 4219-4221.

[16] (a) Oja, S. M.; Robinson, D. A.; Vitti, N. J.; Edwards, M. A.; Liu, Y.; White, H. S.; Zhang. B. Observation of Multipeak collision behavior during the electro-oxidation of single Ag nanoparticles. *J. Am. Chem. Soc.* **2017**, *139*, 708-718; (b) Robinson, D.; Liu, Y.; Edwards, M. A.; Vitti, N. J.; Oja, S. M.; Zhang, B.; White. H. S. Collision dynamics during the electrooxidation of individual silver nanoparticles. *J. Am. Chem. Soc.* **2017**, *139*, 16923-16931.

[17] (a) Ustarroz, J.; Kang, M.; Bullions, E.; Unwin. P. R. Impact and oxidation of single silver nanoparticles at electrode surfaces: one shot *versus* multiple events. *Chem. Sci.* **2017**, *8*, 1841-1853; (b) Ying, Y.-L.; Ding, Z.; Zhan, D.; Long. Y.-T. Advanced electroanalytical chemistry at nanoelectrodes. *Chem. Sci.* **2017**, *8*, 3338-3348.

[18] Sun, T.; Wang, D.C.; Mirkin, M. V. Tunneling mode of scanning electrochemical microscopy: probing electrochemical processes at single nanoparticles. *Angew. Chem. Int. Ed.* **2018**, *57*, 7463-7467.

[19] (a) Glasscott, M.W.; Dick, J.E. Fine-tuning porosity and time-resolved observation of the nucleation and growth of single platinum nanoparticles. *ACS Nano* **2019**, *13*, 4572-4581; (b) Glasscott, M.W.; Pendergast, A.D.;Dick, J.E. A universal platform for the electrodeposition of ligand-free meatl nanoparticles from a water-in-oil emulsion system. *ACS Appl. Nano Mater.* **2018**, *1*, 5702-5711; (c) Li, Y.; Deng, H.; Dick, J.E.; Bard, A.J. Analyzing benzene and cyclohexane emulsion droplet collisions on ultramicroelectrodes. *Anal. Chem.* **2015**, *87*, 11013-11021.

[20] Cresce, A. V.; Russell, S.; Baker, D. R.; Gaskell, K.; Xu, K. In situ and quantitative characterization of solid electrolyte interphases. *Nano Lett.* **2014**, *14*, 1406-1412.

[21] Lutz, L.; Dachraoui, W.; Demortière, A.; Johnson, L. R.; Bruce, P. G.; Grimaud, A.; Tarascon, J.-M. Operando monitoring of the solution mediated discharge and charge processes in a Na-O2 battery using liquid-electrochemical transmission electron microscopy. *Nano Lett.* **2018**, *18*, 1280-1289.

[22] Wang, W. Imaging the chemical activity of single nanoparticles with optical microscopy. *Chem. Soc. Rev.* **2018**, *47*, 2485-2508

[23] Byers, C. P.; Hoener, B. S.; Chang, W.-S.; Link, S.; Landes, C. F. Single-Particle Plasmon Voltammetry (spPV) for Detecting Anion Adsorption. *Nano Lett.* **2016**, 16, 2314-2321.

[24] Liu, T.; Liu, S.; Jiang, W.; Wang, W. Tracking sub-nanometer shift in the scattering centroid of single gold nanorods during electrochemical charging. *ACS Nano* **2019**, *13*, 6279-6286.

[25] Willets, K. A. Supercharging superlocalization microscopy: how electrochemical charging of plasmonic nanostructures uncovers hidden heterogeneity. *ACS Nano* **2019**, *13*, 6145-6150.

[26] (a) Fang, Y.; Wang, W.; Wo, X.; Luo, Y.; Yin, S.; Wang, Y.; Shan, X.; Tao, N. Plasmonic imaging of electrochemical oxidation of single nanoparticles. *J. Am. Chem. Soc.* **2014**, *136*, 12584-12587; (b) Linlin, S.; Fang, Y.; Li, Z.; Wang, W.; Chen, H.-Y. Simultaneous optical and electrochemical recording of single nanoparticle electrochemistry. *Nano Res.* **2017**, *5*, 1740-1748. (c) Linlin, S.; Wang, W.; Chen, H.-Y. Dynamic nanoparticle-substrate contacts regulate multipeak behavior of single silver nanoparticle collisions. *ChemElectroChem* **2018**, *5*, 2995-2999;

[27] Hao, R.; Fan, Y.; Zhang. B. Imaging dynamic collision and oxidation of single silver nanoparticles at the electrode/solution interface. *J. Am. Chem. Soc.* **2017**, *139*, 12274-12282.

[28] (a) Brasiliense, V.; Patel, A. N.; Martinez-Marrades, A.; Shi, J.; Chen, Y.; Combellas, C.; Tessier, G.; Kanoufi, F.Correlated electrochemical and optical detection reveals the chemical reactivity of individual silver nanoparticles. *J. Am. Chem. Soc.* **2016**, *138*, 3478-3483; (b) Patel, A. N.; Martinez-Marrades, A.; Brasiliense, V.; Koshelev, D.; Besbes, M.; Kuszelewicz, R.; Combellas, C.; Tessier, G.; Kanoufi, F. Deciphering elementary steps of transport-reaction processes at individual Ag nanoparticles by 3D superlocalization microscopy. *Nano Lett.* **2015**, *15*, 6454-6463; (c) Lemineur, J.-F.; Stockmann, T. J.; Médard, J.; Smadja, C.; Combellas, C.; Kanoufi, F. Optical nanoimpacts of dielectric and metallic nanoparticles on gold surface by reflectance microscopy: adsorption or bouncing? *J. Anal. Test.* **2019**, *3*, 175-188.

[29] (a) Hill, C.; Pan, S. A dark-field scattering spectroelectrochemical technique for tracking the electrodeposition of single silver nanoparticles. *J. Am. Chem. Soc*. **2013**, 135, 17250-17253; (b) Lemineur, J.-F.; Noël, J.-M.; Ausserré, D.; Combellas, C.; Kanoufi, F. Combining electrodeposition and optical Microscopy for probing size-dependent single-nanoparticle electrochemistry. *Angew. Chem. Int. Ed*. **2018**, 57, 11998-12002; (c) Lemineur, J.-F.; Noël, J.-M.; Combellas, C.; Ausserré, D.; Kanoufi, F. The promise of antireflective gold electrodes for optically monitoring the electro-deposition of single silver nanoparticles. *Faraday Discuss.* **2018**, 210, 381-395.

[30] (a) Wonner, K.; Evers, M. V.; Tschulik K. Simultaneous opto- and spectro-electrochemistry: reactions of individual nanoparticles uncovered by dark-field microscopy. *J. Am. Chem. Soc*. **2018**, *140*, 12658-12661; (b) Brasiliense, V.; Berto, P.; Combellas, C.; Kuszelewicz, R.; Tessier, G.; Kanoufi, F. Electrochemical transformation of individual nanoparticles revealed by coupling microscopy and spectroscopy. *Faraday Discuss*. **2016**, *193*, 339-352; (c) Wonner, K.; Evers, M. V.; Tschulik, K. The electrochemical dissolution of single silver nanoparticles enlightened by hyperspectral dark-field microscopy. *Electrochim. Acta*, **2019**, 301, 458-464.

[31] (a) Brasiliense, V.; Clausmeyer, J.; Dauphin, A. L.; Noël, J.-M.; Berto, P.; Tessier, G.; Schuhmann, W.; Kanoufi, F. Opto-electrochemical In Situ Monitoring of the Cathodic Formation of Single Cobalt Nanoparticles. *Angew. Chem. Int. Ed*. **2017**, 56, 10598-10601; (b) Brasiliense, V.; Clausmeyer, J.; Berto, P., Tessier, G.; Combellas, C.; Schuhmann, W.; Kanoufi, F. Monitoring Cobalt-Oxide Particle Electrochemistry with Subdiffraction Accuracy. *Anal. Chem*. **2018**, 90, 7341-7348.

[32] Sundaresan, V.; Monaghan, J. W.; Willets. K. A. Visualizing the effect of partial oxide formation on single silver nanoparticle electrodissolution. *J. Phys. Chem. C* **2018**, 122, 3138-3145.

[33] (a) Jing, C.; Rawson, F. J.; Zhou, H.; Shi, X.; Li, W.-H.; Li, D.-W.; Long, Y.-T. New insights into electrocatalysis based on plasmon resonance for the real-time monitoring of catalytic events on single gold nanorods. *Anal. Chem*. **2014**, 86, 5513-5518; (b) Jing, C.; Gu, Z.; Long, Y.-T. Imaging electrocatalytic processes on single gold nanorods. *Faraday Discuss*. **2016**, 193, 371-385.

[34] Hao, R.; Fan, Y.; Howard, M. D.; Vaughan, J. C.; Zhang, B. Imaging nanobubbles nucleation and hydrogen spillover during electrocatalytic water splitting. *Proc. Natl. Acad. Sci. U.S.A*. **2018**, 115, 5878-5883.

[35] (a) van Dijk, M. A.; Lippitz, M.; Orrit, M. Far-field optical microscopy of single metal nanoparticles. *Acc. Chem. Res.* **2005**, *38*, 594-601; (b) Lindfors, K.; Kalkbrenner, T.; Stoller, P.; Sandoghdar, V. Detection and spectroscopy of gold nanoparticles using supercontinuum white light confocal microscopy. *Phys. Rev. Lett.* **2004**, *93*, 037401; (c) Sevenler, D.; Avci, O.; Ünlü, M. S. Quantitative interferometric reflectance imaging for the detection and measurement of biological nanoparticles. *Biomed. Opt. Express* **2017**, *8*, 2976-2989; (d) Boccara, M.; Fedala, Y.; Bryan, C. V.; Bailly-Bechet, M.; Bowler, C.; Boccara, A. C. Full-field interferometry for counting and differentiating aquatic biotic nanoparticles: from laboratory to *Tara* Oceans. *Biomed. Opt. Express* **2016**, *7*, 3736-3746.

[36] See https://refractiveindex.info/ last accessed 12-20-2018.

[37] Byers, C. P.; Zhang, H.; Swearer, D. F.; Yorulmas, M.; Hoener, B. S.; Huang, D.; Hoggard, A.; Chang, W.-S; Mulvaney, P.; Ringe, E.; Halas, N. J.; Nordlander, P.; Link, S.; Landes, C. F. From tunable core-shell nanoaprticles to plasmonic drawbridges: active control of nanoparticle optical properties. *Sci. Adv*. **2015**, *1*, e1500988.

[38] Abeyweera, S. C.; Rasamani, K. D.; Sun, Y. Ternary Silver Halide Nanocrystals. *Acc. Chem. Res*. **2017,** 50, 1754-1761.

[39] Andersson, A.; Thomas, J. The source of first-cycle capacity loss in $LiFePO_4$, *J. Power Sources* **2001**, *97–98*, 498-502.

[40] Alonso, C.; Salvarezza, R. C.; Vara, J.M.; Arvia, A.J. The mechanism of silver(I) oxide formation on polycrystalline silver in alkaline solution. Determination of nucleation and growth rates. *Electrochim. Acta* **1990**, *35*, 489-496.

[41] Mirkin, M. V.; Arca, M.; Bard A. J. Scanning electrochemical microcopy. 22. Examination of thin solid silver(I) bromide films : ion diffusion in the film and heterogenous kinetics at the film/solution itnerface. *J Phys Chem.* **1993**, *97*, 10790-10795.

[42] (a) Savéant, J.-M. Molecular catalysis of electrochemical reactions. Mechanistic aspects. *Chem. Rev.* **2008**, *108*, 2348-2378 ; (b) Andrieux, C. P.; Dumas-Bouchiat, J.M.; Savéant, J.-M. Catalysis of electrochemical reactions at redox polymer electrodes. Effect of the film thickness. *J. Electroanal. Chem.* **1980**, *114*, 159-163 ; (c) Anson, F.C. Kinetic behavior to be expectedfrom outer-sphere redox catalysts confined within polymeric films on electrode surfaces. *J. Phys. Chem.* **1980**, *84*, 3336-3338.

[43] Le, H.; Lin, C.; Kätelhön, E.; Compton, R. G. Single-entity electrochemistry: Diffusion controlled transport of an analyte inside a particle. *Electrochim. Acta* **2019**, *298*, 778-787.

[44] Li, Z.; Sun, Y. Silver chlorobromide nanoparticles with highly pure phases: synthesis and characterization. *J. Mater. Chem. A* **2013**, 1, 6786-6793.

[45] Krause, K. J.; Brings, F.; Schnitker, J.; Kätelhön, E.; Rinkin, P.; Mayer, D.; Compton, R. G.; Lemay, S. G.; Offenhäusser, A.; Wolfrum, B. The influence of supporting ions on the electrochemical detection of individual silver nanoparticles: understanding the shape and frequency of current transients in nano-impacts. *Chem. Eur. J*. **2017**, 23, 4638-4643.

[46] (a) The codes developed by Ünlü[35c] for SP-IRIS are available online at https://github.com/derinsevenler/SP-IRIS-BEM last accessed 12-20-2018; they use the MNPBEM-Matlab toolbox available online at: http://physik.uni-graz.at/mnpbem/ last accessed 12-20-2018 developped by Trügler et al.[4646 b,c] (b) Hohenester, U.; Trügler, A. MNPBEM – A Matlab toolbox for the simulation of plasmonic nanoparticles. *Comput. Phys. Commun*. **2012**, *183*, 370-381; (c) Waxenegger, J.; Hohenester, U.; Trügler, A. Plasmonics simulations with the MNPBEM toolbox : Consideration of substrates and layer structures. *Comput. Phys. Commun.*, **2015**, *193*, 138-150.

[47] Baffou, G.; Bon, P.; Savatier, J.; Polleux, J.; Zhu, M.; Mendin, M.; Rigneault, H.; Monneret, H. Thermal imaging of nanostructures by quantitative optical phase analysis. *ACS Nano* **2012**, *6*, 2452-2458.

[48] (a) Yin, B; Huang, X.; Mishra, R.; Sadtler, B. Compositionally-induced twin defects control the shape of ternary silver halide nanocrystals. *Chem. Mater.* **2017**, 29, 1014-1021; (b) Chen, S.; Carey, J. L.; Whitcomb, D. R.; Bühlmann, P.; Penn, R. L. Elucidating the role of AgCl in the nucleation and growth of silver nanoparticles in ethylene glycol. *Cryst. Growth Des.* **2018**, 18, 324-330; (c) Zhang, Y.; Zhang, W.; Wang, L.; Wang, F.; Yang, H. Facile synthesis of AgCl/polydopamine/Ag nanoparticles with in-situ laser improving Raman scattering effect. *Appl. Surf. Sci*. **2017**, 392, 642-648.

[49] Markel, V. A. Introduction to the Maxwell Garnett approximation: tutorial. *J. Opt. Soc. Am. A* **2016**, *33*, 1244-1256.

[50] (a) Crocker, J. C.; Grier, D. G. Methods of Digital Video Microscopy for Colloidal Studies. *J. Colloid Interface Sci*. **1996**, 179, 298-310; (b) Van der Wel, C.; Kraft, D. J. Automated tracking of colloidal clusters with sub-pixel accuracy and precision. *J. Phys.: Condens. Matter*, **2017**, 29, 044001.

[51] (a) Eloul, S.; Kätelhön, E.; Batchelor-McAuley, C.; Tschulik, K.; Compton, R. G. Diffusional nanoimpacts: the stochastic limit. *J. Phys. Chem. C* **2015**, *119*, 14400-14410; (b) Kätelhön, E.; Compton, R. G. Understanding nano-impacts: impact times and near-wall hindered diffusion. *Chem. Sci.* **2014**, *5*, 4592-4598.

[52] Kang, M.; Perry, D.; Kim, Y.-R.; Colburn, A. W.; Lazenby, R. A.; Unwin, P. R. Time-resolved detection and analysis of single nanoparticle electrocatalytic impacts. *J. Am. Chem. Soc*, **2015**, *137*, 10902-10905.

[53] Ustarroz, J.; Ornelas, I. M.; Zhang, G.; Perry, D.; Kang, M.; Bentley, C. L.; Walker, M.; Unwin, P. R. Mobility and Poisoning of Mass-Selected Platinum Nanoclusters during the Oxygen Reduction Reaction. *ACS Catal.* **2018**, *8*, 6775-6790.

[54] Wang, J. Ed. In *Nanomachines: fundamentals and applications*, Wiley-VCH, Weinheim, 2013.

[55] Zhou, C.; Chen, X.; Han, Z.; Wang, W. Photochemically excited, pulsating Janus colloidal motors of tunable dynamics. *ACS Nano* **2019**, *13*, 4064-4072.

Table of Content artwork

